POAC'15

Trondheim, Norway

Proceedings of the 23rd International Conference on
Port and Ocean Engineering under Arctic Conditions
June 14-18, 2015
Trondheim, Norway

OIL SATURATION OF THE SEA ICE PORE SPACE

Sönke Maus[1,4], Jürgen Becker[2], Sabine Leisinger[3], Margret Matzl[3], Martin Schneebeli [3] and Andreas Wiegmann[2]

[1] Dep. of Civil and Transport Engineering, Norwegian University for Science and Technology, Trondheim, NORWAY, email: sonke.maus@sea-ice.no, [2] Math2Market GmbH, Kaiserslautern, GERMANY, [3] WSL Swiss Federal Institute for Snow and Avalanche Research, Davos, SWITZERLAND, [4] Sea Ice Consulting Norway, Trondheim, NORWAY

ABSTRACT

Observations have shown that oil spilled under sea ice collects in patches within the under-ice relief and is encapsulated in the growing ice sheet. Due to its lower density, compared to seawater brine, oil will migrate upwards into the sea ice pore space. During winter migration is limited to lower levels where pore sizes and porosity are larger than near the colder ice surface. Upon warming the oil may continue migration through the widening pore network. To predict when oil may reach the surface, good information about oil saturation, the fraction of the sea ice pore space that may be occupied by oil, is needed. However, at present little is known about the influence on oil saturation and its dependence on sea ice porosity and microstructure. Here we analyse a recently obtained dataset of 3-d X-ray micro-tomographic images of young sea ice to determine oil saturation. We use these images to perform numerical simulations of the immiscible displacement of brine (wetting fluid) by oil (non-wetting) and thereby determine the dependence of oil saturation on porosity and capillary pressure/oil patch thickness. Comparing the results to published observations of laboratory-grown seawater ice of similar age highlights the importance of internal convection for oil entrainment. We perform the analysis for a limited set of 3-d images of older first-year ice of similar porosity. The comparison suggests one to two order higher oil saturation and oil storage capacity in the old ice. To determine the seasonal evolution in the saturation-porosity relationship of oil in sea ice during aging, more observations are needed. This relationship is crucial to estimate the porosity-dependent storage capacity of oil in sea ice, predict oil surfacing, and will be important for planning of response scenarios to oil spills under sea ice.

INTRODUCTION

Oil spilled under a close sea ice cover will, due to its lower density than seawater, rise to the ice-water interface and collect in pools and undulations of the under-ice relief. During the growth season these layers have been found to be encapsulated within the ice as growth continues (Wolfe and Hoult, 1974; Martin, 1979; Fingas and Hollebone, 2003; Otsuka et al., 2004; Karlsson, 2009; Dickins, 2011). Due to its buoyancy the oil will eventually move upwards into the sea ice pore space. Field and laboratory observations indicate that during winter, in cold ice of low porosity, movement is limited to some centimeters from the oil layers, while upon warming, when porosity and pore sizes increase, oil may migrate further upwards, eventually reaching the ice surface.

Based on this scenario, fundamental questions to understand oil spill behavior under ice are:
1.) How much oil may be retained in the under-ice relief?
2.) When does the oil start migrating into the pore space, eventually reaching the surface?
3.) How much oil may be retained in the sea ice pore space?

Several authors have studied aspect 1.) based on high resolution observations of ice thickness (Barnes et al., 1979; Kovacs et al., 1981; Wilkinson et al., 2007) to estimate the under-ice oil pooling or retention capacity in the range of 1 to 6 cm oil layer equivalent[1]. The variability is thought to be related to differences in snow drift pattern (that affect sea ice growth and thickness). Wilkinson et al. (2007) pointed out that considering the flow path of oil into the potential under-ice depressions may lead to an order of magnitude lower estimates of the oil pooling capacity. However, due to lack in observations and concise oil spill and flow modeling studies the topic remains uncertain. Regarding 2.) and 3.), oil migration into the sea ice pore space been observed in the field in a more or less qualitative manner (NORCOR, 1975; Martin, 1979), while only recently quantitative results of oil retention in the pore space have been obtained in laboratory experiments (Otsuka et al., 2004; Karlsson, 2009; Karlsson et al., 2011). These results were use by Petrich et al. (2013) to estimate that oil storage in the pore space of warm ice may roughly account for 20% of the under-ice pooling capacity. This estimate is however based on model assumptions derived from the small-scale laboratory experiments.

In the present study we discuss oil storage capacity in the pore space of natural sea ice, and to what degree the mentioned laboratory experiments are useful to derive this capacity. As a new approach to the problem we evaluate oil entrainment into the sea ice pore space based on 3-d micro-tomographic images of natural sea ice. These images are used to perform numerical simulations of the immiscible displacement of brine by oil in sea ice pore networks. As common in soil mechanics and petroleum engineering, we define oil saturation $\mathcal{S}_{oi}$ as

$$\mathcal{S}_{oi} = \frac{\phi_{oi}}{\phi_{oi} + \phi_b}, \tag{1}$$

where ϕ_{oi} and ϕ_b and are the pore fractions of oil and brine. Hence, $\mathcal{S}_{oi}$ is the fraction of the total pore space occupied by oil, a number between 0 and 1. This definition neglects air inclusions that are not considered accessible to fluid flow of brine or oil. We investigate how the maximum $\mathcal{S}_{oi}$ in sea ice depends on ice porosity and the thickness of oil layers from which the oil drains, as well as on ice type (young and old first-year ice). We then compare our numerical simulations with the mentioned laboratory observations of oil entrainment in young ice (Otsuka et al., 2004; Karlsson, 2009; Petrich et al., 2013), and draw some conclusions about oil saturation in the sea ice pore space of natural sea ice of different age.
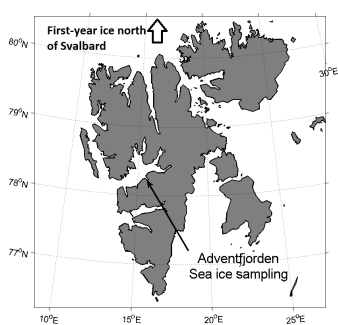
FIELD WORK AND METHODS

Figure 1: Sea ice sampling sites for this study: Young sea ice was obtained by snowscooter from Adventfjorden, thick first year ice during a cruise with R.V. Lance north of Svalbard.
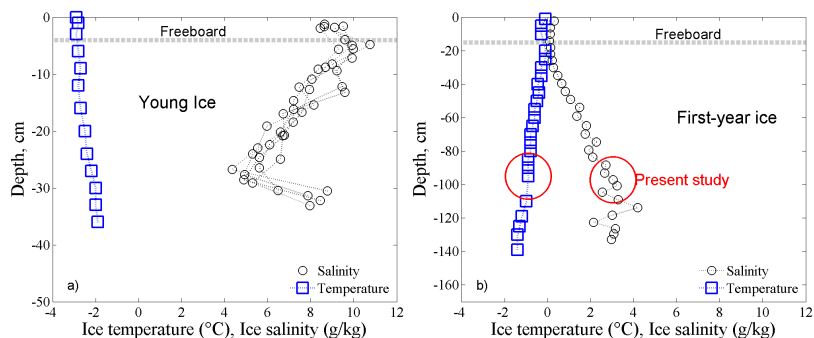
Figure 2: Temperature and salinity profiles of a) young sea ice, approximately 35 cm thick, obtained on 16.03.2011 in Adventbay, Svalbard. b) First-year ice sampled on 24.08.2010 during ICE2010 with R.V. Lance north of Svalbard. First year ice samples investigated in this study stem from different cores, yet having similar properties and distance from the ice-water interface as indicated by the red circle.

---

[1]Other authors have used units L/m^2 and m^3/km^2, yet we prefer the conversion to an equivalent oil layer

Young ice and old first-year ice samples were obtained during field work within and north of the Svalbard Archipelago 2010/2011 (Figure 1). Young fast ice was sampled in Adventbay of Adventfjorden, Svalbard, approximately 2 km from the UNIS (University Courses on Svalbard) building, during 14th to 19th April 2011. Sampling and processing procedures, as well as meteorological conditions, were described in Maus et al. (2013). In summary, the analysis presented here is based on a set of 6 ice cores obtained close to each other (1-2 m) and within an hour from 35 cm thick fast ice. One core was used for temperature profile determination with a penetration probe, the other five cores for salinity and microstructure analysis. Salinity cores were rapidly cut into 3-4 cm thick subsamples, packed into conical lockable plastic beakers and stored in an isolating box. They were, within 30 minutes from the beginning of coring, transported by snow mobile to the UNIS laboratory, where they were stored in temperature-controlled freezers. One core was stored close to its *in situ* temperatures (typically within 0.3 K), while the other cores were gradually cooled to lower values, the coldest samples to -10 °C. After 1-2 days of storage, samples were centrifuged with a refrigerated centrifuge. As for the young ice, we have applied the same procedure - sampling, cooling, centrifugation and processing on samples from 1.0 m thick summer first-year ice, obtained at the end of the melting season during a cruise into the Marginal Ice Zone north of Svalbard (ICE cruise, 16.08-2.09.2010, R/V LANCE). For this ice we did not process the whole core, yet 15 cm segments roughly 0.35 to 0.5 m from the bottom of 5 adjacent cores, which were cut into three 5 cm slices each. Also here the three samples from the first core were stored at their *in situ* temperature, while the other cores were gradually cooled to lower temperatures down to -10 °C, prior to centrifugation. Immediately after centrifugation the ice samples were put in a low temperature freezer at -80 °C. The salinity S_b of the centrifuged brine was obtained with an electric conductivity probe, and its mass m_b measured. Some hours later the mass m_{ir} of the cooled residual ice samples was measured, and the samples were reduced from their initial 7.25 cm to 4 cm diameter. The residual ice that was cut off was melted to obtain its salinity, S_{ir}. From salinity and mass of brine and residual ice, the bulk salinity was obtained as $S_i = (S_b m_b + S_{ir} m_{ir})/(m_b + m_{ir})$.

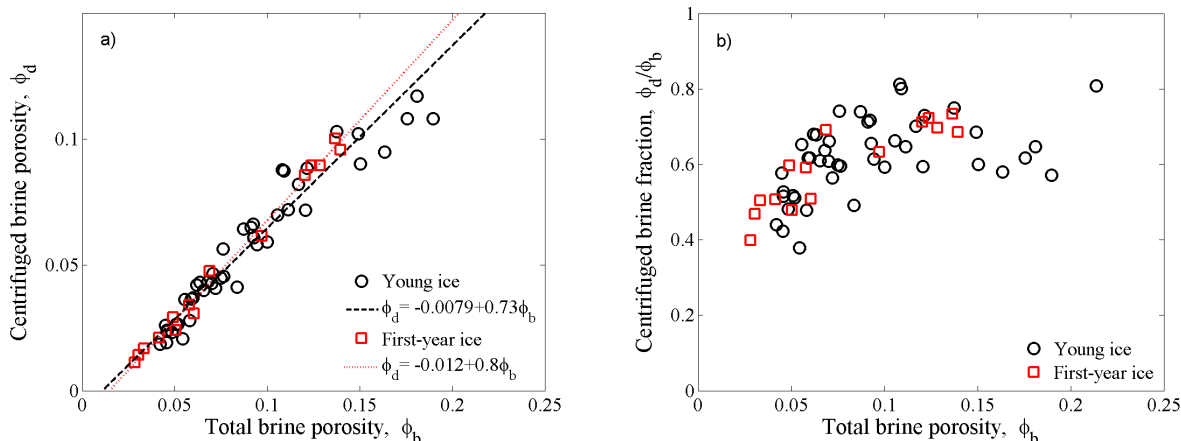## SEA ICE BULK SALINITY AND CENTRIFUGED POROSITY

Figure 3: a) Relationship between centrifuged brine porosity ϕ_d and total brine porosity ϕ_b, for young ice in Adventfjorden (black circles) and first-year ice north of Svalbard (red symbols); b) same data as in a) but plotted as the centrifuged fraction ϕ_d/ϕ_b versus brine porosity ϕ_b to emphasize the expected saturation limit.

Bulk salinity and temperature profiles for young ice and first year ice are shown in Figure 2a. The young ice salinity profile shows the typical C-shape for this kind of ice, with higher salinity towards the surface and the sea ice-water interface. There is little variability between the cores. Hence, all ice cores have similar original macroscopic properties prior to the cooling in the laboratory. This gives us confidence that our cooling experiment will let us find the microstructure dependence of this ice type on temperature and porosity, with minimal scatter due to natural

3

macroscopic variability. The first-year ice properties are shown in Figure 2b on the same scale. It is warmer and less saline, especially at the surface. The depth regime of the first-year ice samples analysed here is indicated by a red circle.

The salinity measurements may be further used to derive the fraction of the brine that was extracted by centrifuging. Let the total brine porosity ϕ_b be the sum of the centrifuged brine porosity ϕ_d and the residual brine porosity ϕ_{ir}. Then, assuming that the corresponding brine salinities are the same, these may be determined from salinity determinations alone. The centrifuged brine porosity ϕ_d is given as

$$\phi_d = 1 - \phi_b \frac{S_{ir}}{S_i} \left(\frac{S_b - S_i}{S_b - S_{ir}} \right), \tag{2}$$

where the total brine porosity ϕ_b was determined from S_i and temperature T_i, assuming thermodynamic equilibrium and applying equations from Cox and Weeks (1983).

The dependence of the centrifuged brine porosity ϕ_d on total brine porosity ϕ_b is shown in Figure 3a for young ice and first-year ice. Both data sets may be approximated by linear relationships shown in the figure (with correlation coefficient R=0.99 for first-year ice data and 0.96 for the young ice). These observations may be taken as an indication of a threshold in ϕ_b where all brine is entrapped, i.e. $\phi_d = 0$. The linear fits imply thresholds $\phi_b(\phi_d = 0) = 0.011$ for the young ice and $\phi_b(\phi_d = 0) = 0.015$ for the first year ice. It is noteworthy that, while the pore size distributions discussed below are very different, the thresholds are similar, and lower than the value of 0.05 that has been suggested based on most previous work (Cox and Weeks, 1988; Golden et al., 1998; Petrich et al., 2006; Golden et al., 2007; Pringle et al., 2009). In Figure 3b the observations are plotted in a different form, emphasizing the fraction ϕ_d/ϕ_b of the total brine porosity ϕ_b that may be extracted by centrifugation, being in the range 40 to 80%. Similar results have been reported in other studies based on centrifuged sea ice samples (Weissenberger et al., 1992; Maus et al., 2011). We expect this fraction ϕ_d/ϕ_b of extractable brine to be an upper limit for the oil saturation $\mathcal{S}_{oi}$.

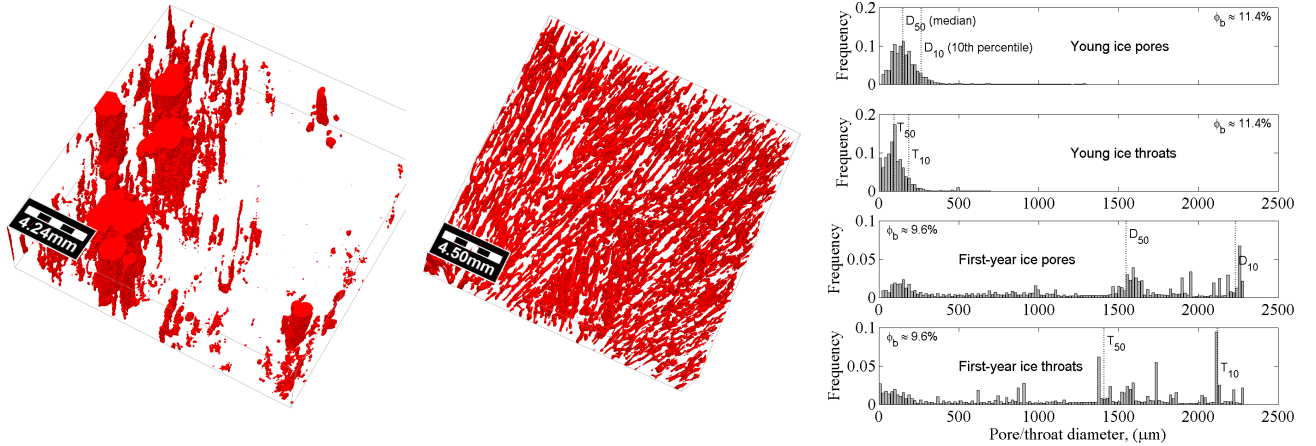## X-RAY MICROTOMOGRAPHIC IMAGING

Figure 4: 3d images, 20 mm on a side and 5.5 mm in height, of pores (red) in first-year ice (left) and young ice (middle) based on X-ray tomography. Right: Corresponding pore and throat size distributions, with median (D_{50},T_{50}) and largest 10 percent diameter (D_{10},T_{10}) indicated as vertical stippled lines.

Non-destructive X-ray 3d tomography (XRT) was first applied by Kawamura (1988) to sea ice, at that time resolution-limited to millimeter-sized pores. While now XRT with voxel size $20 - 40$ μm has been successfully applied to study polar firn and snow (e.g., Freitag et al., 2004; Schneebeli and Sokratov, 2004), an application to sea ice is more difficult. The low absorption contrast between brine and ice is, in contrast to air-ice for snow, is insufficient to obtain good

4

quality images of the pore space. Hence, Golden et al. (2007) added a contrast agent to obtain images of laboratory ice grown from NaCl solutions. This is not feasible in the field. However, our approach to centrifuge samples prior to X-ray imaging circumvents this problem and was shown to yield good image quality of the centrifugable interconnected pore space (Maus et al., 2009).

Imaging was performed at the WSL Swiss Federal Institute for Snow and Avalanche Research, Davos, Switzerland, with two desktop cone-beam microCT instruments (MicroCT 40 and MicroCT 80, Scanco Medical AG) that operate with a microfocus X-ray source (7 μm diameter) and detectors of 2048 x 256 and 2048 x 128 elements, respectively. Young/old ice samples were scanned with a 37/50 mm field of view, yielding a nominal resolution of 18/25 μm. As the samples were scanned with 500 images per 180 degrees rotation, the actual resolution was probably a factor of 1.5 worse. Scanning time was roughly 1 hour per centimeter sample height. The resulting XRT grayscale images were stored as 16-bit stacks, and filtered with ImageJ (rsb.info.nih.gov/ij/), applying a 2 pixel median and Gaussian blur filter (standard deviation 1.5). A global threshold that separates air and ice was found on sub-images with approximately equal fractions of air pores and ice, using by Otsu's (Otsu, 1979) method. From the raw images, including the sample holder, a cylinder with largest possible square cross section was cropped, to obtain vertical rectangular cylinders of typically 2 cm length on a side and 2-2.5 cm in height. These were again subdivided vertically into samples of 5.5 mm height. The subdivision is important for proper determination of permeability and percolation[2], as for 20 mm high samples a considerable fraction (10-30%) of slightly (10 to 30 degrees) inclined pores are running off at the vertical sides. Examples of these 3d sub-images to be analysed here are shown in Fig. 4 for young and first year ice.

For pore space analysis and numerical simulations described below we used GeoDict (2012), "Geometric Material Models and Computational PreDictions of Material Properties". Porosities solely determined from tomography images are denoted with an apostrophe: ϕ'_o is the porosity open to the upper or lower sample surfaces, i.e. it does not include air bubbles (ignoring the bubbles close to the surfaces), but corresponds to the centrifuged brine. Note that neither the entrapped brine porosity is included in ϕ'_o, as we only segmented air and ice. To obtain a total brine porosity estimate based on the tomography images, ϕ'_b, we assume that ϕ'_o resembles the centrifuged porosity ϕ_d of the macroscopic samples, and calculate ϕ'_b from the linear fits in Figure 3a. While this extends the porosity range of the young ice to lower values than for the macroscopic samples, it is noted that the derived values are uncertain below $\phi'_b \approx 0.03$.

PORE SIZE LIMITS FOR OIL ENTRAINMENT

Two types of the pore size distributions were determined with GeoDict (2012),. The first uses a sphere fitting algorithm to determine the fraction of the pore space that belongs to a certain diameter interval, which we term *pore size*. The second is based on the injection of spheres into the sample (here from top and bottom) to determine the fraction of the pore space that can be accessed through a sphere of a given radius. The latter is a *porosimetry* algorithm that determines an effective volume distribution of pores limited by throats, and is termed *throat size* in the following. In Fig. 4 we show pore and throat size volume distributions for the first-year and young ice examples of similar brine porosity. The young ice has a median pore diameter D_{50} of 0.15 mm, the distribution is narrow and 90 % of the pores have diameters less than 0.26 mm (D_{10}). Corresponding pore throat characteristics are about 50% smaller. For the first-year ice the distribution is much broader. As for the young ice, there is a local maximum in the 0.1-0.2 mm range, yet the bulk of the pore diameters are an order of magnitude larger ($D_{50} = 1.5$mm, $D_{10} = 2.2$mm). The pore throat distribution has similar characteristic values ($T_{50} = 1.4$mm, $T_{10} = 2.1$mm), indicating that the effect of pore throats on sample permeability is less for the first-year than for the young ice.

The pore size characteristics (D_{50}, D_{10}, T_{50}, T_{10}) for all samples are shown in Figure 5 in dependence on the tomography-based total brine porosity ϕ'_b. For the young ice, in the figure

---

[2]For the young ice images we presented numerical permeability computations in an earlier paper(Maus et al., 2013)
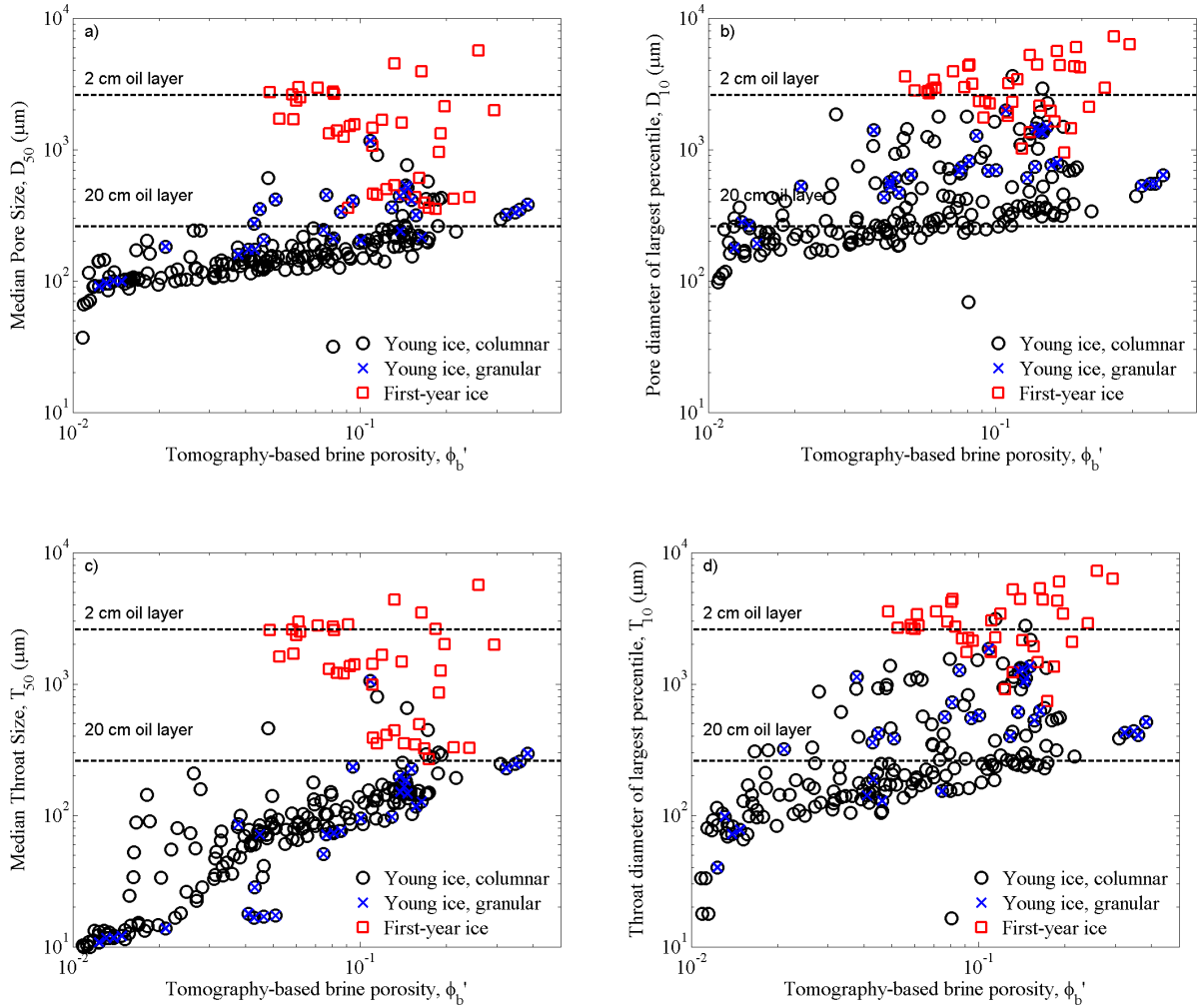
5

Figure 5: Pore characteristics of young and old first year ice in dependence on total brine porosity: b) median pore diameter D_{50} of the pore space distribution; b) pore diameter D_{10} dividing the largest 10th percentile (by volume) of the pore space distribution; c) median throat diameter T_{50}, defined as the pore size through which 50 % of the pore space can be accessed from the top and bottom surfaces distribution; d) T_{10}, the the pore size through which 10 % of the pore space can be accessed from the top and bottom surfaces. For the young ice columnar and granular samples are distinguished in the legend. The horizontal lines represent the critical entrance capillary diameter for oil drainage for pressures corresponding to oil layers of thickness 2 and 20 cm.

it is distinguished between granular (within 3-4 cm from the ice surface, shown as blue x), and columnar ice samples. In general it is seen that, while for the young ice the characteristic pore sizes are all found to decrease with brine porosity, for the old first-year ice (red squares) the data are more scattered. These pore sizes are an order of magnitude larger than for young ice.

For a further discussion of the difference we evaluate the pore size distributions in terms of the potential of oil entrainment into sea ice. to do so, we consider a capillary from which a wetting fluid (seawater brine) is displaced by a non-wetting fluid (oil), a process that is often called *drainage* (Sahimi, 1993, e.g.,). The conditions for drainage may be addressed in terms of the Young-Laplace equation for the capillary pressure P_c:

$$P_c = \sigma_{nw} cos(\theta) \left(\frac{1}{R_1} + \frac{1}{R_2} \right), \tag{3}$$

where R_1 and R_2 are the principle radii of curvature, σ_{nw} is the oil-water surface tension and θ the oil-ice contact angle. In the following we simplify this for capillaries with circular cross section, for which the right hand factor becomes $2/R$. We are primarily interested in the case when oil is spilled below sea ice and collects there at layer thickness H. Having a lower density than brine, the oil experiences a buoyancy force, with a buoyancy-induced pressure due to the oil layer of

6

$P_b = H\Delta\rho g$, where $\Delta\rho$ is the density difference of crude oil and water and g gravity acceleration. The condition for drainage to occur, $P_c = P_b$, then corresponds to

$$H = \frac{2\sigma_{nw}cos(\theta)}{g\Delta\rho R}. \tag{4}$$

Inserting characteristic properties $\sigma_{nw} \approx 0.02$ J/m^2 (Malcolm and Dutton, 1979), a contact angle of 180°, and a density difference $\Delta\rho \approx 160$ kg/m^3 of crude oil and seawater brine[3] yields

$$H \approx 2.6 \times 10^{-5}/R, \tag{5}$$

where both H and R are in meters. Equation (5) may then be interpreted in the following manner: When a 10 mm oil layer is released below sea ice, its buoyancy will be sufficient to overcome the capillary pressure and enter pores that have a diameter of more than 5.2 mm. The relationship (5) has been plotted in Figure 5 as horizontal lines, to illustrate the potential of oil drainage in connection with the characteristic pore sizes. The lines indicating the regime between a 2 cm (upper line) and 20 cm oil layer (lower line). These values have been chosen as they represent the average and maximum oil layer thickness observed during NORCOR (1975). Note that, for data points that fall above these lines, the respective oil layers are sufficiently thick to enter these pores.

Figure 5a shows the pore size median D_{50}. For young ice, with the narrow pore size distribution, it corresponds closely to the maximum in the pore size histogram (see Fig. 4), and may be taken as an average characteristic of the pore space. Most of the data for D_{50} fall below the 20 cm oil layer line, which means that even for rather thick oil layers the pores in young ice are not accessible for the oil (when only buoyancy forces are considered). In contrast, the pores in old first year ice are accessible, and for half of the samples this even applies to an oil layer thickness of only 2 cm. A more stringent limit is obtained from the median throat size T_{50} (Figure 5c), which takes into account how throats constrain the accessible pore space. This effect appears to be particularly relevant for the granular young ice samples. Whereas the pores in granular young ice appear wider than for columnar samples (Figure 5a), one observes very similar relationships for the throats. For the old first year ice the throat median T_{50} is only slightly lower than the pore median D_{50}, and the constraints on pores accessibility do not change much.

Furthermore, in Figures 5b and d we show D_{10} and T_{10} which are a measure of the pore size of the 10% largest pores. With the more stringent throat size criterion one finds that, for a 20 cm oil layer, oil may enter 10% of the pores for most granular samples, but only to some degree for the columnar samples. A 2 cm oil layer would be insufficient for oil to enter even the 10% largest pores in young ice, while for most old first-year ice samples it is sufficient.

SIMULATION OF OIL-WATER DISPLACEMENT

While the characteristic pore sizes serve as a first estimate to decide if oil may enter the brine filled pores in sea ice, it does not provide quantitative data on the fraction of the pore space that may be occupied by oil during its drainage, i.e. the oil saturation $\mathcal{S}_{oi}$. In particular, we are interested in the dependence of $\mathcal{S}_{oi}$ on the oil layer thickness H. To estimate this dependence we used the GeoDict package SatuDict, that offers the possibility to obtain a saturation-dependent capillary pressure curve (which in our case is converted to a saturation dependent oil layer thickness curve). In SatuDict the saturation $\mathcal{S}_{oi}$ is, similar to the sphere fitting and porosimetry algorithms, obtained by evaluating the distribution of non-wetting (oil) and wetting (brine) phases for a variety of capillary pressures. GeoDict offers the choice between several displacement models for imbibition (corresponding to brine displacing oil) and drainage (oil displaces brine). In the model applied here (Hilpert and Miller, 2001) the invading non-wetting phase (oil) is connected to a reservoir and displaces the wetting phase (brine) starting at one given spatial direction.

---

[3]$\Delta\rho$ depends on oil type and the range for oil from Northern Seas is roughly 80-190 kg/m^3 with respect to standard seawater at its freezing point (e.g., Karlsson, 2009), and somewhat larger (120-230 kg/m^3) for brine with a freezing point of -5 °C
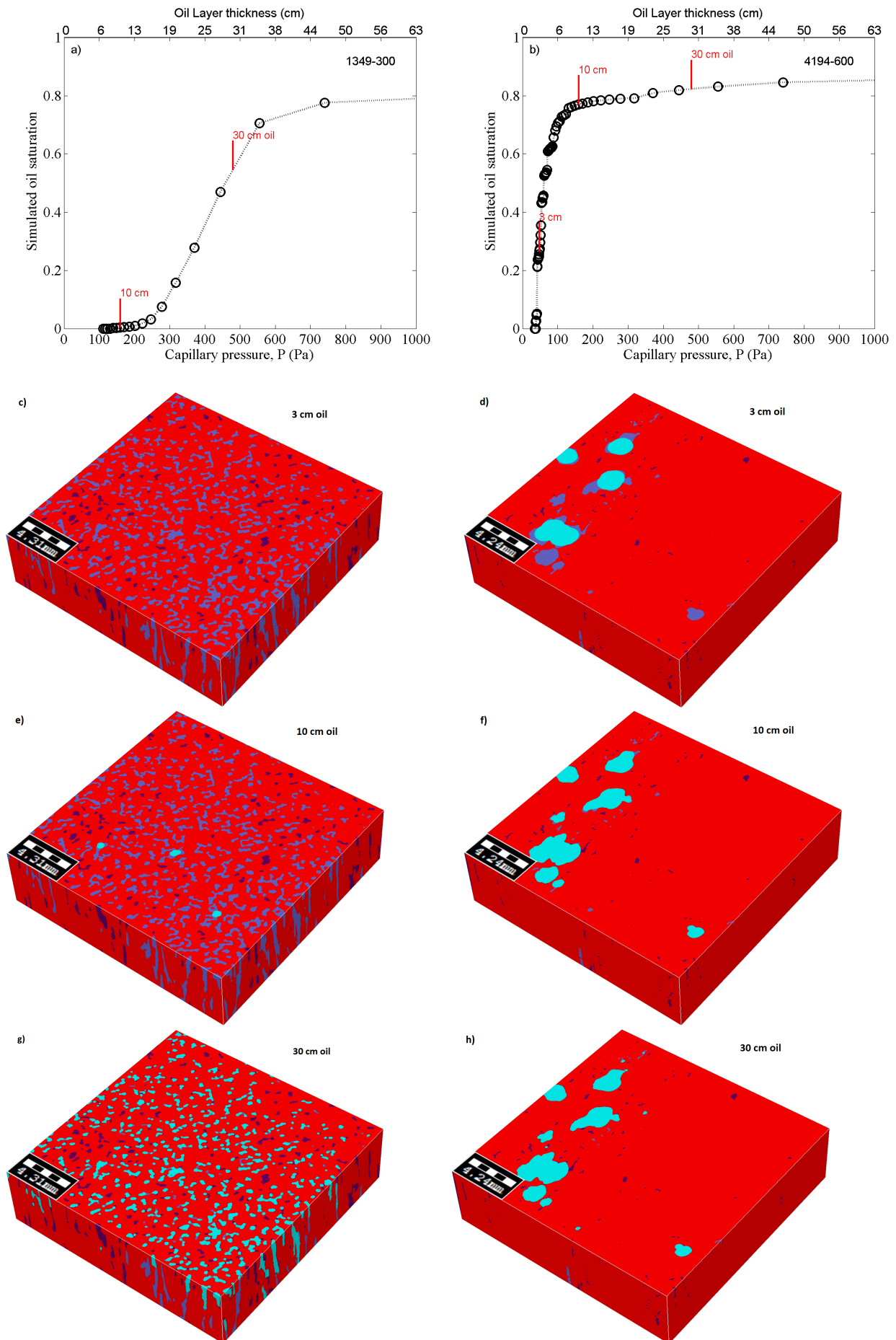
Figure 6: Immiscible displacement of oil in young (left) and first-year (right) sea ice: a) and b) dependence of saturation on capillary pressure/oil layer thickness; c)-h) 3-d images of oil (cyan) and brine (blue) distribution for different oil layer thicknesses 3, 10 and 30 cm. The dark blue/magenta coloring denotes the residual brine that cannot be displaced through oil injection from the top, as the pores are not connecting through the sample.

The results of these simulation are illustrated for a young ice and a first-year ice sample in Figure 6. The upper Figures 6a and b show the simulated saturation in dependence on capillary pressure/oil layer thickness, while the figures below compare the 3-d distribution of oil for three oil layer thicknesses 3, 10 and 30 cm. Note that in the figure the oil is injected from the top, but that this in nature corresponds to injection from below, as the 3-d images are shown flipped up-down. As already suspected and discussed in connection with Figure 5, the saturation curve shows that for young ice little oil entrainment can be expected in case of oil layers being less than 20 cm thick (if the drainage is driven by oil-brine buoyancy difference alone). For the first-year ice, Figure 6b shows that there is a steep increase in saturation while the oil layer thickness increases to 6 cm, whereas a further increase does not add much to the oil saturation. While saturation curves, determined for all samples show some scatter (to be discussed in the final section), the results in Figure 6 are representative for all young and old-first year ice samples of the present study.

DISCUSSION

To discuss our simulations with respect to observations, we first revise the available observational data on oil saturation. Karlsson et al. (2011) have summarised laboratory experiments, own work as well as from Otsuka et al. (2004), and shown these data as the relationship of oil porosity ϕ_{oi} and total porosity ϕ_t (their Figure 4). For our purpose we plot the data of these studies in terms of the relationship of oil saturation $\mathcal{S}_{oi}$ versus total porosity in Figure 7a. The laboratory experiments typically lasted from a few days to three weeks, resulting in ice thicknesses of 6 to 27 cm. The ice may thus be comparable to our young ice from the field. For older first year ice, there is clearly a lack in quantitative data of oil content in ice. The only published measurement known to us is from the NORCOR experiment (NORCOR, 1975; Martin, 1979), where an average oil volume of 4.5% has been reported as an average for the spring season. While the corresponding average total porosity has not been reported, we can estimate the latter based on the published salinity and temperature profiles. Assuming that ϕ_t was in the range 9 to 13 %, we estimate the single red square shown in Figure 7a along with the laboratory data (as black circles and triangles with green and blue additional coding). The single NORCOR value appears at the upper limit of the laboratory data.

In the next Figures 7b-f we show for comparison the oil saturation estimated for our microscopic samples in dependence on sample total porosity ϕ_t. The values have been extracted from the saturation-capillary pressure curves (as in Figures 6a and b) for oil layer thicknesses of 1, 3, 10 and 30 cm, and infinite pressure (corresponding to maximum saturation). For young ice (black circles) we again distinguish granular (additional blue crosses) and columnar samples, while first-year ice results are shown as red squares. The strong dependence of saturation on oil layer thickness is evident in particular for young ice.

Apparently, for a comparison with our simulations, the oil layer thickness in the observations is relevant: Karlsson (2009) reported values of a few millimeters for his experiments, while the tank geometry and released oil volumes reported by Otsuka et al. (2004) may be used to estimate oil layers in the range 2 to 7 mm. These numbers imply that the laboratory observations in Figure 7a are to be compared to the simulated saturation for a 1 cm oil layer in Figures 7b. However, according to the latter Figure, one would not expect any oil to migrate into the young ice pore space. Does this mean, that the laboratory ice has a fundamentally different microstructure than the ice form the field? On the one hand, such difference has not been described Weeks (2010); on the other hand, one finds from Figure 7b that not even the first-year ice pore space is expected to entrain considerable oil amounts for an oil layer of 1 cm. The discrepancy is probably related to another process not accounted in the simulations: oil drainage is not only governed by buoyancy forces alone, but also forced by convection. Strong convective desalination of sea ice takes place in particular in the high porosity, few centimeters thick *skeletal layer* near the ice-water interface (Weeks, 2010). Indeed, for the NORCOR experiments it has been reported that ice within 10 to 20 mm from the interface became heavily oiled, while further penetration through a few wider pores
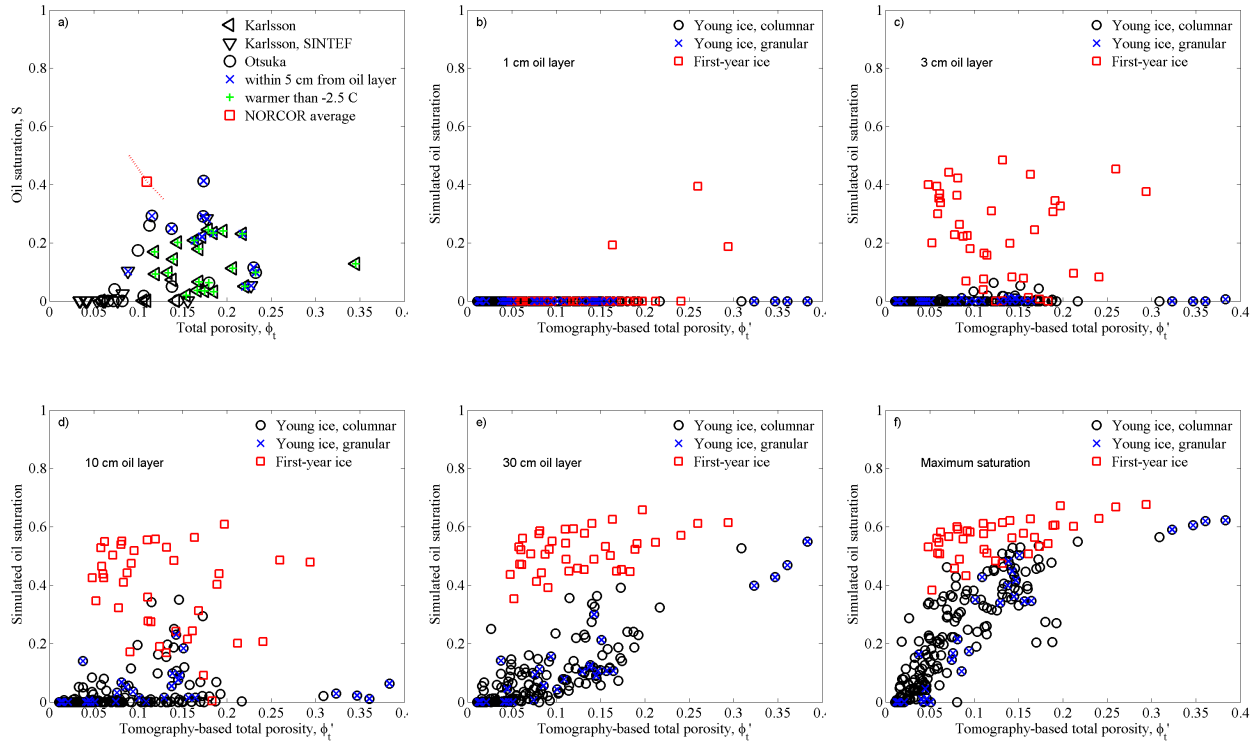
Figure 7: Oil saturation versus total porosity: a) laboratory observations summarised by Karlsson et al. (2011) shown as triangles and circles, as well as an average value estimated for the NORCOR experiment (NORCOR, 1975); b-f) Simulated oil saturation based on micro-tomographic young ice (circles) and old first-year ice samples (red squares) for oil layer thicknesses of 1, 3, 10 and 30 cm, as well as infinite pressure (corresponding to maximum saturation).

was normally restricted to within 5 to 10 cm from the oil layers (NORCOR, 1975; Martin, 1979). As most oil-containing laboratory ice samples stem from close to the oil release layers (within 5 cm, see legend), and sample vertical resolution was not better than 2 to 5 cm, it is plausible that most of the data points in Figure 7a are strongly influenced by the contribution from this skeletal layer. Another effect that may play a role, is convection driven by surface melt as discussed by Martin (1979), as half of the laboratory data are taken after a warming period. We indicate this possibility by depicting the warmest samples in Figure 7a.

Considering the only field observation in Figure 7a, the corresponding average oil layer thickness reported for NORCOR in spring is about 4.5 cm (NORCOR, 1975), but oil layers in unequally distributed pools may have been larger. The value should thus be compared to our simulations for 3 or 10 cm oil layer thickness (Figures 7c and d). Agreement is reasonable, considering that the NORCOR observation is an estimate for many cores. The average value compares reasonably to the simulated saturations for 3 and 10 cm oil layers at corresponding porosity.

Based on the simulations, it does not appear that a porosity threshold for oil entrainment of 10 to 15% total porosity, as proposed based on the laboratory data (Karlsson et al., 2011; Petrich et al., 2013), is justified. When only young ice is considered, Figure 7b to f illustrates that such a threshold would strongly depend on oil layer thickness and corresponding pressure to overcome capillary forces. Also, the comparison with laboratory observations in Figure 7a suggests that oil entrainment in the reported laboratory experiments must have been governed by convection in the skeletal layer (and/or due to surface melting). Observations of this convective entrainment are presently lacking, e.g., the low vertical resolution of the laboratory observations has not resolved this regime. It thus remains unclear if oil entrainment in young ice may be approximated by a simple constant skeletal layer approach. To make progress for young ice requires both 3-d modeling and observations of convectively driven brine-oil displacement in the sea ice skeletal layer. For older first-year ice, Figure 7b to f implies a weaker dependence of oil entrainment on oil layer thickness, yet also here a porosity threshold is not evident, at least not for porosities above 5% as

resolved here.

In summary, comparing young ice and first-year ice results indicates that, in addition to oil layer thickness and convection processes, ice type and age (and respective pore sizes) are critical for oil in ice entrainment. To make progress the most important step appears to be to obtain good observations of pore space evolution during the transition from young ice to first-year ice.

CONCLUSIONS

We have performed numerical pore-scale simulations with 3-d microtomographic sea ice images to estimate the immiscible displacement of brine by oil. The simulations lead us to the following conclusions:
1. The oil layer thickness is fundamental to predict oil drainage into old first-year ice, where buoyancy (oil-brine density difference) is likely a sufficient driver to overcome capillary forces.
2. Simulations for young ice indicate that buoyancy is insufficient to drive oil into the pore networks, and there is a need to better understand convection as the likely driving force.
3. We do not find a porosity threshold for oil entrainment into sea ice. Rather there are other factors (ice age and pore space, oil layer thickness, convection) that control the process.

The comparison of our numerical simulations with laboratory experiments on oil release has also revealed the need for more systematic observations. Provided that field data of first-year ice of different age and growth conditions are obtained, the micro-tomographic method may then have the potential to establish the relationship of oil saturation, total porosity and oil layer thickness for known ice growth conditions and thermal history. While time-consuming, the pore-scale method has the considerable advantage that it reduces the amount of environmentally harmful spill experiments to investigate the problem.

To link the pore-scale results to large scale observations and predictions, it is an important question how the sea ice bottom relief, as well as the under-ice flow of oil constrain the maximum oil layer thickness. E.g., while (Dickins, 2011) suggested a simple scaling of 10% of the level ice thickness for the oil pool depth, several studies indicate that both sea ice deformation and snow drift need to be understood on the floe scale to make reliable predictions of potential oil pools (Barnes et al., 1979; Kovacs et al., 1981), highlighting the importance of high resolution ice thickness and under-ice relief data (Wilkinson et al., 2007).

REFERENCES

Barnes, P. W., Reimnitz, E., Toimil, L., Hill, H., 1979. Fast ice thickness and snow depth in relation to oil entrapment potential, prudhoe bay, alaska. Tech. rep., U.S. Geol. Survey, open-file report 79-539.

Cox, G. F. N., Weeks, W. F., 1983. Equations for determining the gas and brine volumes of sea ice samples during sampling and storage. J. Glaciol. 32, 371–375.

Cox, G. F. N., Weeks, W. F., 1988. Numerical simulations of the profile properties of undeformed first-year ice during the growth season. J. Geophys. Res. 93 (C10), 12449–12460.

Dickins, D., 2011. Behavior of oil spills in ice and implications for Arctic spill response. In: Proceedings of the OTC Arctic Technology Conference, OTC 22126. pp. 1–15, Houston, Texas, USA.

Fingas, M. F., Hollebone, B. P., 2003. Review of behaviour of oil in freezing environments. Mar. Poll. Bulletin 47, 333–340.

Freitag, J., Wilhelms, F., Kipfstuhl, S., 2004. Microstructure-dependent densification of polar firn derived from X-ray microtomography. J. Glaciol. 50 (169), 243–259.

GeoDict, 2012. (Geometric material models and computational preDictions of material properties). Web: www.geodict.com.

Golden, K. M., Ackley, S. F., Lytle, V. I., 1998. The percolation phase transition in sea ice. Science 282, 2238–2241.

Golden, K. M., Heaton, H. E. A., Miner, J., Pringle, D. J., Zhu, J., 2007. Thermal evolution of permeability and microstructure in sea ice. Geophys. Res. Lett. 34, L16501.

Hilpert, M., Miller, C., 2001. Pore-morphology-based simulation of drainage in totally wetting porous media. Adv. Water Resour. 24, 243–255.

Karlsson, J., 2009. Oil movement in sea ice. Master's thesis, University of Copenhagen, enmark, 199pp.

Karlsson, J., Petrich, C., Eicken, H., 2011. Oil entrainment and migration in laboratory-grown saltwater ice. In: Proceedings of the 21st International Conference on Port and Ocean Engineering underArctic Conditions 10-14 July 2011. pp. 1–10, montreal, Canada. POAC11-186,.

Kawamura, T., 1988. Observations of the internal structure of sea ice by X Ray computed tomography. J. Geophys. Res. 93 (C3), 2343–2350.

Kovacs, A., Morey, R. M., Cundy, D. F., Decoff, G., July 1981. Pooling of oil under sea ice. In: Proceedings - Port and Ocean Engineering under Arctic Conditions, Quebec City. POAC, pp. 912–922.

Malcolm, J., Dutton, C., 1979. The interfacial tension and contact angle of crude oil under ice. Port and Ocean Engineering under Arctic Conditions , 771–778Norwegian Institute of Technology.

Martin, S., 1979. A field study of brine drainage and oil entrainment in first-year sea ice. J. Glaciol. 22 (88), 473–502.

Maus, S., Haase, S., Büttner, J., Huthwelker, T., Schwikowski, M., Vähätalo, A., Enzmann, F., 2011. Ion fractionation in young sea ice from Kongsfjorden, Svalbard. Annals Glaciol. 52 (57), 301–310.

Maus, S., Huthwelker, T., Enzmann, F., Miedaner, M. M., Stampanoni, M., Marone, F., Hutterli, M. A., Ammann, M., Hintermüller, C., Kersten, M., 2009. Synchrotron-based X-ray tomography: insights into sea ice microstructure. In: Leppäranta, M. (Ed.), Rep. Ser. Geophys., University of Helsinki. Vol. 61. 28-45.

Maus, S., Leisinger, S., Matzl, M., Schneebeli, M., Wiegmann, A., June 2013. Modelling oil entrapment in sea ice on the basis of microtomographic images. In: Proceedings - Port and Ocean Engineering under Arctic Conditions, Espoo, Finland. POAC, 10 pp.

NORCOR, 1975. The interaction of crude oil with Arctic sea ice. Vol. Technical Report No. 27 of Beaufort Sea Project. Department of Environment, Victoria, BC, Canada, 201 pp.

Otsu, N., 1979. A threshold selection method from gray-level histograms. IEEE Transactions on Systems, Man and Cybernetics SMC-9 (1), 62–66.

Otsuka, N., Kondo, H., Saeki, H., 2004. Experimental study on the characteristics of oil ice sandwich. Proceedings of OCEANS '04 3, 1470–1475.

Petrich, C., Karlsson, J., Eicken, H., 2013. Porosity of growing sea ice and potential for oil entrainment. Cold Reg. Sci. Technol. .

Petrich, C., Langhorne, P. J., Sun, Z. F., 2006. Modelling the interrelationships between permeability, effective porosity and total porosity in sea ice. Cold Reg. Sci. Techn. 44, 131–144.

Pringle, D. J., Miner, J. E., Eicken, H., Golden, K. M., 2009. Pore space percolation in sea ice single crystals. J. Geophys. Res. 114.

Sahimi, M., 1993. Flow phenomena in rocks. Rev. of Mod. Phys. 65 (4), 1393–1534.

Schneebeli, M., Sokratov, S. A., 2004. Tomography of temperature gradient metamorphism of snow and associated changes in heat conductivity. Hydrol. Processes 18, 3655–3665.

Weeks, W. F., 2010. On Sea Ice. University of Alaska Press.

Weissenberger, J., Dieckmann, G., Gradinger, R., Spindler, M., 1992. Sea ice: A cast technique to examine and analyze brine pockets and channel structure. Limnol. Ocean. 37 (1), 179–183.

Wilkinson, J. P., Wadhams, P., Hughes, N. E., 2007. Modelling the spread of oil under fast sea ice using three-dimensional multibeam sonar data. Geophys. Res. Letters 34, L22506.

Wolfe, L. S., Hoult, D. P., 1974. Effects of oil under sea ice. J. Glaciol. 13 (69), 473–488.